

Article

CO₂ Hydrogenation on Ni_xMg_{1-x}Al₂O₄: A Comparative Study of MgAl₂O₄ and NiAl₂O₄

Boseok Seo ^{1,†}, Eun Hee Ko ^{1,†}, Jinho Boo ¹, Minkyu Kim ^{1,*}, Dohyung Kang ^{1,*} and No-Kuk Park ^{2,*}

¹ School of Chemical Engineering, Yeungnam University, 280 Daehak-ro, Gyeongsan 38541, Gyeongbuk, Korea; qhseokk1469@naver.com (B.S.); rhdmngml0809@naver.com (E.H.K.); qnwlsg123@naver.com (J.B.)

² Institute of Clean Technology, Yeungnam University, 280 Daehak-ro, Gyeongsan 38541, Gyeongbuk, Korea

* Correspondence: mk_kim@ynu.ac.kr (M.K.); dkang@ynu.ac.kr (D.K.); nokukpark@ynu.ac.kr (N.-K.P.)

† B.S. and E.H.K. contributed equally.

Abstract: Due to the increasing attention focused on global warming, many studies on reducing CO₂ emissions and developing sustainable energy strategies have recently been performed. One of the approaches is CO₂ methanation, transforming CO₂ into methane. Such transformation (CO₂ + 4H₂ → CH₄ + 2H₂O) provides advantages of carbon liquification, storage, etc. In this study, we investigated CO₂ methanation on nickel–magnesium–alumina catalysts both experimentally and computationally. We synthesized the catalysts using a precipitation method, and performed X-ray diffraction, temperature-programmed reduction, and N₂ adsorption–desorption tests to characterize their physical and chemical properties. NiAl₂O₄ and MgAl₂O₄ phases were clearly observed in the catalysts. In addition, we conducted CO₂ hydrogenation experiments by varying with temperatures to understand the reaction. Our results showed that CO₂ conversion increases with Ni concentration and that MgAl₂O₄ exhibits high selectivity for CO. Density functional theory calculations explained the origin of this selectivity. Simulations predicted that adsorbed CO on MgAl₂O₄(100) weakly binds to the surface and prefers to desorb from the surface than undergoing further hydrogenation. Electronic structure analysis showed that the absence of a *d* orbital in MgAl₂O₄(100) is responsible for the weak binding of CO to MgAl₂O₄. We believe that this finding regarding the origin of the CO selectivity of MgAl₂O₄ provides fundamental insight for the design methanation catalysts.

Keywords: CO₂ methanation; CO₂ hydrogenation; CO₂ conversion; nickel aluminate; magnesium aluminate



Citation: Seo, B.; Ko, E.H.; Boo, J.; Kim, M.; Kang, D.; Park, N.-K. CO₂ Hydrogenation on Ni_xMg_{1-x}Al₂O₄: A Comparative Study of MgAl₂O₄ and NiAl₂O₄. *Catalysts* **2021**, *11*, 1026. <https://doi.org/10.3390/catal11091026>

Academic Editor: Paraskevi Panagiotopoulou

Received: 3 August 2021

Accepted: 23 August 2021

Published: 24 August 2021

Publisher's Note: MDPI stays neutral with regard to jurisdictional claims in published maps and institutional affiliations.



Copyright: © 2021 by the authors. Licensee MDPI, Basel, Switzerland. This article is an open access article distributed under the terms and conditions of the Creative Commons Attribution (CC BY) license (<https://creativecommons.org/licenses/by/4.0/>).

1. Introduction

The amount of fossil fuel used worldwide continues to increase, and the resulting greenhouse gas emissions are now known to represent a major global challenge. The minimization of CO₂ emitted from fossil-based energy sources is a priority, and renewable energy production units such as solar, wind, and geothermal energy plants are actively being installed [1]. Although solar power is now considered as one of the most economically competitive energy resources, large-scale investment is still needed to replace fossil-based energy for massive-scale energy production [2]. Given this scenario, the use of fossil fuels coupled with CO₂ capture and utilization offers a near-term solution that meets the need for economically sustainable energy [3].

CO₂ capture, utilization, and sequestration (CCUS) technology can provide a means of sustainable fossil-based energy use [4]. In terms of the large-scale CO₂ utilization, CO₂ can be hydrogenated to produce CH₄ (by methanation; CO₂ + 4H₂ → CH₄ + 2H₂O) [5] which can be readily liquified, transported, and stored. In addition, CO, a central intermediate for Fischer–Tropsch and methanol synthesis, can also be produced from CO₂ hydrogenation (by reverse water gas shift (RWGS); CO₂ + H₂ → CO + H₂O) [6].

Depending on reaction conditions used for CO₂ hydrogenation, CO₂ can be converted into CH₄ or CO by methanation or RWGS, respectively [7], although based on considera-

tions of the scope of CH₄ utilization and existing natural gas infrastructure, methanation is preferred.

Group 8 to 10 metals such as Ni, Ru, Rh, Co, and Fe are catalytically active with respect to CO₂ hydrogenation [8,9]. Among these metals, nickel is preferred as an active catalyst metal because it is cheaper than Ru or Rh. The particle size of nickel strongly determines its selectivity for CO₂ hydrogenation products produced by methanation or RWGS [10]. For example, it has been reported that smaller nickel particles favor high CO selectivity, whereas larger particles are more selective toward CH₄ [11]. The mechanism of CO₂ hydrogenation is believed to proceed via the hydrogenation of a surface-adsorbed intermediate [12]. CO₂ is adsorbed on nickel and dissociates into CO, which is strongly adsorbed and further dissociated into atomic carbon that is hydrogenated to form CH₄ [13]. On the other hand, weakly adsorbed CO can desorb into the gas phase [14,15]. In addition to the direct dissociation of CO₂ on nickel, the dissociation of H₂ and the resulting atomic hydrogen can facilitate the dissociation of C–O bonds. This hydrogen-assisted mechanism has been reported by observing the formation of formates and carbon hydroxyl species on a nickel-based catalyst [7].

Alumina has widely been used as a support for nickel catalysts due to its moderate price, high surface area, and ability to resist high temperatures. Although nickel-on-alumina catalysts are highly efficient for CO₂ methanation, nickel tends to be dissolved into the alumina to form nickel aluminate (NiAl₂O₄; spinel structured). The catalytic activity of nickel for CO₂ methanation is greater than nickel aluminate; therefore, efforts have been made to suppress the formation of nickel aluminate [16]. MgO was added to nickel–alumina catalysts to minimize nickel aluminate formation, but magnesium aluminate was generated [17]. The addition of Mg can boost the basicity of the alumina support and suppress carbon deposition during CO₂ hydrogenation, whereas higher Ni content promotes higher selectivity for CO₂ methanation due to the dissociation of H₂ on the Ni⁰ site [18]. When MgO is added to nickel–alumina catalysts, three possibly active structures for CO₂ hydrogenation may be formed, viz., nickel, nickel aluminate, and magnesium aluminate.

The role played by nickel in CO₂ hydrogenation is well understood in terms of particle size [10] and metal–reactant intermediate reactions [19]. It has also been reported that oxygen vacancies in NiAl₂O₄ promote the dissociation of CO₂ to CO [20] and facilitate the hydrogenation of adsorbed CO to atomic carbon. However, little is known of the role of magnesium aluminate on CO₂ hydrogenation. In this study, we explored the use of nickel and magnesium aluminates catalysts for CO₂ hydrogenation, experimentally and computationally.

The following questions are addressed in this article: (1) What are properties of the nickel–magnesium–alumina catalysts synthesized by co-precipitation?; (2) Are nickel and magnesium aluminates active CO₂ hydrogenation catalysts?; (3) What is the reaction mechanism responsible for CO₂ hydrogenation on nickel and magnesium aluminate?

2. Experimental Section

2.1. Synthesis of Ni_xMg_{1-x}Al₂O₄ Catalysts

Ni_xMg_{1-x}Al₂O₄ catalysts were prepared by co-precipitation. Stoichiometric amounts of metal nitrate precursors (Ni(NO₃)₂·6H₂O (Sigma-Aldrich ≥ 99.0%), Mg(NO₃)₂·6H₂O (Sigma-Aldrich ≥ 99.0%), and Al(NO₃)₃·9H₂O (Sigma-Aldrich ≥ 98.0%)) were dissolved in deionized water, stirred for 1 h, and treated with ammonium bicarbonate ((NH₄)HCO₃, (Sigma-Aldrich ≥ 99.0%)) dropwise to a pH of 7. Solid precipitates were then aged overnight and filtered. The cake obtained was washed with deionized water 5 times, dried for 24 h at 100 °C, crushed, and calcined at 900 °C under atmospheric conditions overnight. The calcined powder was then pulverized in a ball mill using high-purity alumina balls. The final product was named Ni_xMg_{1-x}Al₂O₄, where the subscript ‘x’ is the molar ratio of Ni to Mg.

2.2. Catalytic Activity Tests

Catalytic activity for CO₂ hydrogenation was measured using an experimental setup similar to one previously reported [16]. Catalyst powder (5.0 g) was vertically loaded with quartz wool into a fixed bed reactor (inner diameter 1/2 inch) mounted in a 3-zone furnace. Initially, the catalyst was heated to the reaction temperature at 10 °C/min under 800 sccm N₂ flow. The temperature of each heating zone was precisely monitored, and the flow rate of the gas mixture was controlled using a mass flow controller (MFC). The reactant gas CO₂:H₂:N₂ (ratio 1:4:6.5 vol/vol) was then supplied at 1013 sccm into the heated reactor. WHSV (weight hourly space velocity) was set to ~12,000 mL·g^{−1}·h^{−1}. Steam in the effluent gas was condensed out using a cold trap, and the dried product gas mixture was monitored online using a gas chromatograph (Donam, DS6200) equipped with a thermo conductivity detector and gas analyzer with an infrared sensor (ABB-AO2000). CO₂ conversion, CH₄ selectivity, and CO selectivity were calculated as follows.

$$\text{CO}_2 \text{ conversion} = \frac{F_{\text{CO}_2 \text{ in}} - F_{\text{CO}_2 \text{ out}}}{F_{\text{CO}_2 \text{ in}}}$$

$$\text{CH}_4 \text{ selectivity} = \frac{F_{\text{CH}_4 \text{ out}}}{F_{\text{CO}_2 \text{ in}} - F_{\text{CO}_2 \text{ out}}}$$

$$\text{CO selectivity} = \frac{F_{\text{CO out}}}{F_{\text{CO}_2 \text{ in}} - F_{\text{CO}_2 \text{ out}}}$$

where F_i is the volumetric flow rate of species i (sccm).

2.3. Characterization of Catalysts

Crystalline structures of catalysts were analyzed by powder X-ray diffraction (XRD, nickel-filtered CuK α radiation, 40.0 kV and 15.0 mA, Miniflex, Rigaku, Japan) using a scanning range from 10° to 90° and a scanning rate of 10°/min. Temperature-programmed reduction (TPR) by H₂ was measured by chemisorption (BELCAT-B, MICROTRAC, Japan). Before measurements, samples were degassed at 300 °C under flowing Ar for 30 min and cooled to 30 °C at the same Ar flow rate. For TPR, samples (50 mg) were heated from 100 to 900 °C at 10 °C/min under a flowing Ar/10 vol.% H₂ mix. Effluent gas was monitored using a thermal conductivity detector.

2.4. Computation Details

All plane-wave DFT calculations were performed using projector-augmented wave pseudopotentials [21] provided in the Vienna ab initio simulation package (VASP) [22]. The Perdew–Burke–Ernzerhof (PBE) [23] exchange–correlation was used with a plane-wave expansion cutoff of 400 eV. We used the dispersion-corrected DFT-D3 [24] method for all calculations. Due to the magnetic moment of MgAl₂O₄, we performed spin-polarized calculations for MgAl₂O₄ but nonspin-polarized calculations for NiAl₂O₄. We employed the spinel structures of MgAl₂O₄ and NiAl₂O₄ which were dominantly observed by XRD. The PBE bulk lattice constants of MgAl₂O₄ ($a = b = c = 8.16$ Å) and NiAl₂O₄ ($a = b = c = 8.14$ Å) were used to fix the lateral dimensions of MgAl₂O₄ and NiAl₂O₄ slabs, respectively. In recent theoretical study using molecular dynamic simulation, the spinel structure of MgAl₂O₄ favorably has a low index facet of (100). In addition, the (100) surface is predicted to easily undergo surface re-constructions to be more stabilized [25]. However, we only focused our computational studies on the pristine (100) surface for both slabs to explore the intrinsic reactivity of MgAl₂O₄(100) and NiAl₂O₄(100) surfaces. Simulated MgAl₂O₄(100) and NiAl₂O₄(100) slabs consisted of 4 layers with two fixed bottom layers, but other layers were allowed to relax until the forces were less than 0.03 eV/Å. Both surfaces of MgAl₂O₄(100) and NiAl₂O₄(100) had coordinatively unsaturated (cus) surface metal sites and cus oxygen atoms. The MgAl₂O₄(100) surface with Mg_{cus}, Al_{cus}, and O_{cus} surface atoms is shown in Figure 1a, and the NiAl₂O₄(100) surface with Ni_{cus}, Al_{cus} and O_{cus} sites is shown in Figure 1b. All computational slab models included a vacuum spacing of ~20 Å,

which was sufficient to reduce periodic interaction in the surface normal direction. In terms of system size, 2×2 (MgAl_2O_4) and 2×2 (NiAl_2O_4) unit cells with corresponding $2 \times 2 \times 1$ Monkhorst–Pack k-point meshes were employed. Unless otherwise noted, our DFT calculations were performed for a single molecule adsorbed within the surface models, and it corresponds to coverages equal to 25% and 50% of the total density of Al_{cus} metal atoms and cus metal atoms of Mg and Ni, respectively. Although NiO and Ni were also observed from the XRD experiment, we did not investigate Ni and NiO computationally because it has been extensively studied and proposed to be very active toward CO_2 hydrogenation [8,9,16].

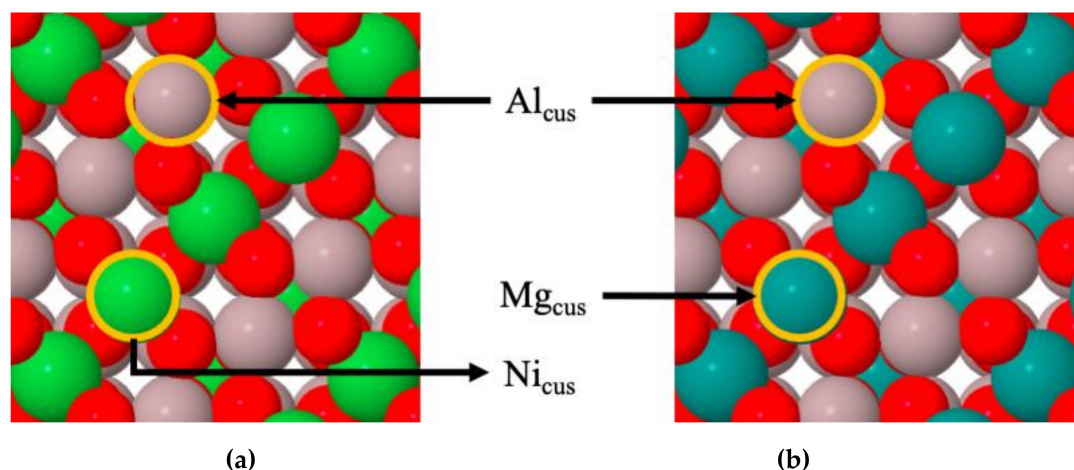


Figure 1. Top views of the $\text{NiAl}_2\text{O}_4(100)$ and $\text{MgAl}_2\text{O}_4(100)$ surfaces. The cus on $\text{NiAl}_2\text{O}_4(100)$ and $\text{MgAl}_2\text{O}_4(100)$ represent coordinatively unsaturated sites. Red atoms are oxygens and metal atoms are labeled.

We defined the adsorption energy between molecule and surface as Equation (1), where E_{slab} , E_{iso} , and $E_{\text{slab+ads}}$ are energies of the bare surface, an isolated molecule, and an adsorbed molecule on the bare surface, respectively. A larger positive adsorption energy value indicated high stability of the adsorbed molecule under consideration.

$$E_{\text{ads}} = E_{\text{slab}} + E_{\text{iso}} - E_{\text{slab+ads}} \quad (1)$$

We evaluated the activation energy barriers for initial steps of methanation on surfaces using the climbing nudged elastic band (cNEB) method [26], and confirmed that the resulting transition states had one imaginary vibrational frequency. All energies reported in this paper are corrections of zero-point vibrational energy.

Projected crystal orbital Hamilton population (pCOHP) has been used to characterize and quantify the interactions between orbitals of CO and $\text{Metal}_{\text{cus}}$ [27–29]. pCOHP provides a measure of the overlap between specific atomic orbitals, and therefore, a relative quantification of bonding. LOBSTER software was used to obtain pCOHP values from VASP outputs [30].

3. Experimental Results

3.1. Characterization of Catalysts

XRD was used to determine the crystalline structures of $\text{Ni}_x\text{Mg}_{1-x}\text{Al}_2\text{O}_4$ catalysts (Figure 2a). For $\text{Ni}_1\text{Mg}_0\text{Al}_2\text{O}_4$, peaks were located at 37.3° , 43.3° , and 63° , which corresponded to the crystalline NiO phase. Other peaks near 37.5° , 45.3° , 60.2° , and 66.1° represented the crystalline NiAl_2O_4 phase. After adding Mg to the $\text{Ni}_1\text{Mg}_0\text{Al}_2\text{O}_4$ catalyst to produce $\text{Ni}_{0.75}\text{Mg}_{0.25}\text{Al}_2\text{O}_4$, peaks related to MgAl_2O_4 were observed in the XRD pattern and the intensities of NiO-related peaks diminished. Increasing the amount of Mg enhanced MgAl_2O_4 peak intensities until only MgAl_2O_4 peaks were observed. XRD patterns indicated that crystalline NiO and NiAl_2O_4 phases were predominantly formed in

Ni-rich catalysts and that the addition of Mg into $\text{Ni}_1\text{Mg}_0\text{Al}_2\text{O}_4$ resulted in the formation of a crystalline MgAl_2O_4 phase rather than NiAl_2O_4 .

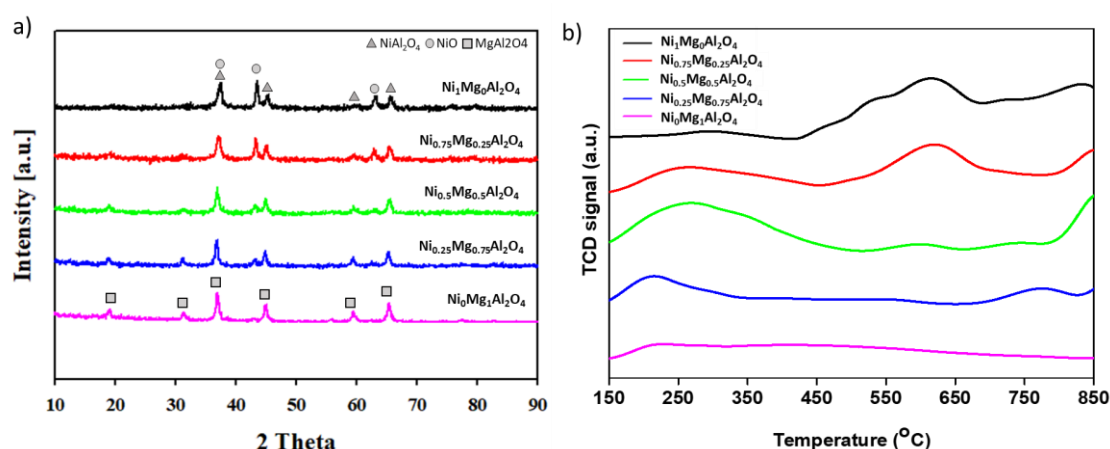


Figure 2. (a) XRD patterns and (b) H_2 -TPR curves of $\text{Ni}_x\text{Mg}_{1-x}\text{Al}_2\text{O}_4$ catalysts.

The reduction characteristics of $\text{Ni}_x\text{Mg}_{1-x}\text{Al}_2\text{O}_4$ catalysts were evaluated by H_2 -TPR (Figure 2b). The NiO phase of Ni-included catalysts started to be reduced around 250 °C, i.e., Ni was formed at the temperature used for CO_2 hydrogenation experiments. This reduction may have been due to the reduction of NiO to Ni, whereas the band observed at ~600 °C was attributed to the reduction of NiAl_2O_4 in $\text{Ni}_1\text{Mg}_0\text{Al}_2\text{O}_4$ and $\text{Ni}_{0.75}\text{Mg}_{0.25}\text{Al}_2\text{O}_4$, which corresponded to that reported in a previous study [31], in which almost-complete reductions of NiO and NiAl_2O_4 were observed below 700 °C. $\text{Ni}_{0.5}\text{Mg}_{0.5}\text{Al}_2\text{O}_4$ and $\text{Ni}_{0.25}\text{Mg}_{0.75}\text{Al}_2\text{O}_4$ which had a MgAl_2O_4 spinel rather than NiAl_2O_4 showed weak reduction bands between 600 and 750 °C due to the minor NiAl_2O_4 phase. On the other hand, reduction bands were hardly observed in H_2 -TPR of $\text{Ni}_0\text{Mg}_1\text{Al}_2\text{O}_4$. Based on XRD patterns and TPR curves, we speculated that the crystalline NiAl_2O_4 and MgAl_2O_4 structures of $\text{Ni}_x\text{Mg}_{1-x}\text{Al}_2\text{O}_4$ catalysts could not be fully reduced during CO_2 hydrogenation at 450 °C.

Textural properties of $\text{Ni}_x\text{Mg}_{1-x}\text{Al}_2\text{O}_4$ catalysts were evaluated using N_2 adsorption-desorption isotherms (Figure 3). All catalysts had similar isotherm type V with a hysteresis curve around a relative pressure of 0.8 due to high metal loading and the high calcination temperature used (900 °C). Surface areas, total pore volumes, and average pore sizes were quantified from N_2 isotherms (Table 1). Despite the different compositions of $\text{Ni}_x\text{Mg}_{1-x}\text{Al}_2\text{O}_4$ catalysts, textural properties were not noticeably different except for $\text{Ni}_{0.75}\text{Mg}_{0.25}\text{Al}_2\text{O}_4$, presumably because the same alumina support was used and all were calcined at 900 °C. The larger surface area and total pore volume of $\text{Ni}_{0.75}\text{Mg}_{0.25}\text{Al}_2\text{O}_4$ might increase the catalytic activity for CO_2 hydrogenation. However, for other catalysts, the observation of similar textural properties given different crystalline structures implies that different catalytic activities for CO_2 hydrogenation were predominantly due to the different NiAl_2O_4 and MgAl_2O_4 crystalline structures of $\text{Ni}_x\text{Mg}_{1-x}\text{Al}_2\text{O}_4$ catalysts.

Table 1. Textural properties of $\text{Ni}_x\text{Mg}_{1-x}\text{Al}_2\text{O}_4$ catalysts.

Sample	Surface Area (m^2/g)	Total Pore Volume (mL/g)	Average Pore Size (nm)
$\text{Ni}_1\text{Mg}_0\text{Al}_2\text{O}_4$	38.0	0.17	10.8
$\text{Ni}_{0.75}\text{Mg}_{0.25}\text{Al}_2\text{O}_4$	64.2	0.26	11.4
$\text{Ni}_{0.5}\text{Mg}_{0.5}\text{Al}_2\text{O}_4$	38.1	0.13	9.4
$\text{Ni}_{0.25}\text{Mg}_{0.75}\text{Al}_2\text{O}_4$	32.8	0.10	8.4
$\text{Ni}_0\text{Mg}_1\text{Al}_2\text{O}_4$	32.1	0.10	8.2

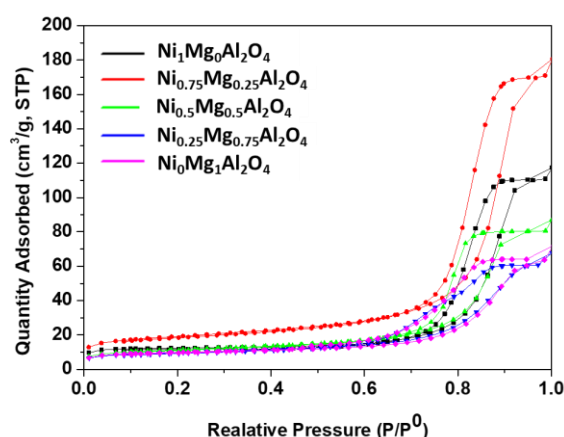


Figure 3. BET results of $\text{Ni}_x\text{Mg}_{1-x}\text{Al}_2\text{O}_4$ catalysts.

3.2. CO_2 Hydrogenation Activity

CO_2 hydrogenation was conducted over $\text{Ni}_x\text{Mg}_{1-x}\text{Al}_2\text{O}_4$ catalysts to examine the different catalytic characteristics of NiAl_2O_4 and MgAl_2O_4 spinel structures. More specifically, H_2 and CO_2 conversions were measured versus temperature over $\text{Ni}_x\text{Mg}_{1-x}\text{Al}_2\text{O}_4$ catalysts (Figure 4a,b). Despite the exothermic nature of CO_2 methanation, H_2 and CO_2 conversion increased with temperature for all catalysts because reactions were conducted using a kinetically controlled regime. Regarding the effects of catalyst compositions, H_2 and CO_2 conversion tended to increase with the Ni composition. For example, whereas $\text{Ni}_0\text{Mg}_1\text{Al}_2\text{O}_4$, which mainly consisted of MgAl_2O_4 , achieved CO_2 and H_2 conversions of 3.6 and 11.2%, respectively, at 450 °C, $\text{Ni}_1\text{Mg}_0\text{Al}_2\text{O}_4$, which was composed of NiO and NiAl_2O_4 , achieved 39.8 and 42.5%, respectively. It has been widely reported that the presence of the metallic Ni, which can be partially reduced from NiO , is an excellent catalyst for CO_2 hydrogenation [32]. A number of studies have investigated the catalytic activities of NiAl_2O_4 and MgAl_2O_4 for CO_2 hydrogenation [16].

To understand the mechanisms responsible for the catalytic effects of NiAl_2O_4 and MgAl_2O_4 , we calculated molar ratios of H_2 to CO_2 consumed (Figure 4c). This molar ratio is theoretically four, based on the stoichiometry of CO_2 methanation, but one for RWGS. As nickel content increased, the molar ratio of consumed H_2 to CO approached four, suggesting that CH_4 methanation predominated over Ni and NiAl_2O_4 . In contrast, as the Ni content decreased, the molar ratio approached one, indicating that RWGS predominated over MgAl_2O_4 .

We also measured CO selectivity versus the Mg content of $\text{Ni}_x\text{Mg}_{1-x}\text{Al}_2\text{O}_4$ catalysts (Figure 4d) to confirm the different reaction behaviors of NiAl_2O_4 and MgAl_2O_4 (Figure 4c). As was expected, CO selectivity increased with the increasing Mg content. In particular, the CO selectivity of $\text{Ni}_{0.5}\text{Mg}_{0.5}\text{Al}_2\text{O}_4$ was much greater than that of $\text{Ni}_{0.75}\text{Mg}_{0.25}\text{Al}_2\text{O}_4$. This might be due to their distinct crystalline structures, whereas in the XRD patterns of $\text{Ni}_{0.75}\text{Mg}_{0.25}\text{Al}_2\text{O}_4$, NiO and NiAl_2O_4 , MgAl_2O_4 peaks predominated in the XRD pattern of $\text{Ni}_{0.5}\text{Mg}_{0.5}\text{Al}_2\text{O}_4$ (Figure 2a). Considering the enhanced CO selectivity of $\text{Ni}_{0.75}\text{Mg}_{0.25}\text{Al}_2\text{O}_4$ and its distinct MgAl_2O_4 structure, we speculated that the MgAl_2O_4 structure promoted RWGS. The detailed reaction mechanisms of MgAl_2O_4 and NiAl_2O_4 were further investigated by computational study.

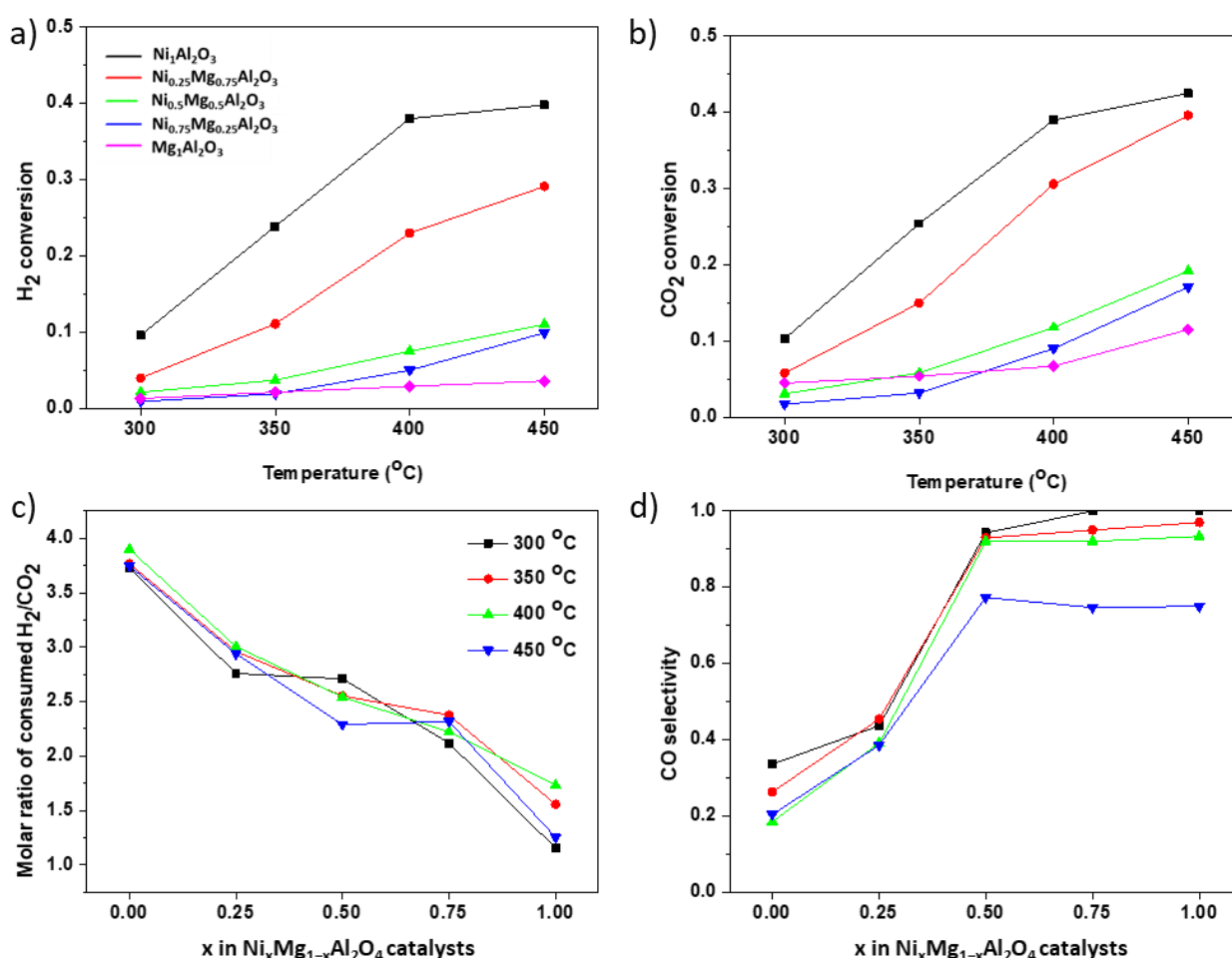


Figure 4. Results of catalytic activity tests for CO₂ hydrogenation over Ni_xMg_{1-x}Al₂O₄ catalysts, (a) H₂ conversion versus temperature, (b) CO₂ conversion versus temperature, (c) molar ratio of consumed H₂/CO₂ versus X for Ni_{1-x}Mg_xAl catalysts, and (d) CO selectivity versus X for Ni_{1-x}Mg_xAl catalysts.

4. Computational Results

4.1. Stabilities of CO₂ and CO on MgAl₂O₄(100) and NiAl₂O₄(100)

To understand the CO₂ methanation mechanism, we evaluated adsorbed CO₂ stability on MgAl₂O₄(100) and NiAl₂O₄(100). DFT predicted the most favorable configurations of adsorbed CO₂ on both surfaces are shown in Figure 5; the corresponding adsorption energies are provided below each configuration in the figure. We also tested other sites and other configurations of CO₂, but the configurations shown in Figure 5 were predicted to be the most energetically favorable. Our simulations predict that adsorbed CO₂ on Mg_{cus} site is more stable than the CO₂ on the Al_{cus} site on the MgAl₂O₄(100) surface. The linear configuration of CO₂ on the Mg_{cus} site transformed to the bent configuration during DFT relaxation. In contrast to the Mg_{cus} site, the linear CO₂ weakly bound with an adsorption energy of 5.3 kJ/mol on the Al_{cus} site (not shown), for which the energy barrier of transformation from linear CO₂ to bent CO₂ was predicted to be negligible. This implies that because the linear CO₂ easily transforms to bent CO₂ on the Al_{cus} site by overcoming the negligible barrier, the bent CO₂ would predominate at these sites. In general, CO₂ tends to bind weakly on catalytic surfaces [33–38], but our results show that CO₂ binds strongly at both cus sites with large adsorption energies. Methanation includes CO formation; therefore, we also investigated CO stability on cus sites of MgAl₂O₄(100) and NiAl₂O₄(100). Our simulations predict that on MgAl₂O₄(100), CO adsorption on the Mg_{cus} site is energetically more favorable than on other sites, but that adsorbed CO is much less stable than adsorbed CO₂. These results suggest that adsorbed CO generated from

initial C–O bond cleavage in CO₂ readily desorbs from the surface of MgAl₂O₄, which supports its observed high selectivity toward CO during CO₂ methanation.

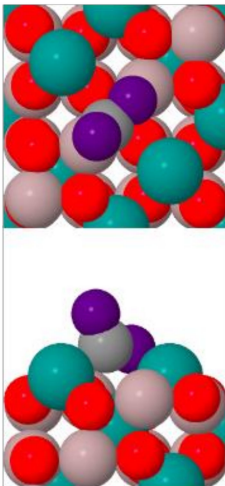
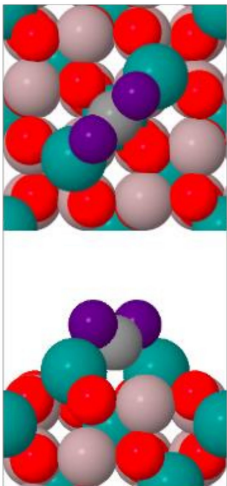
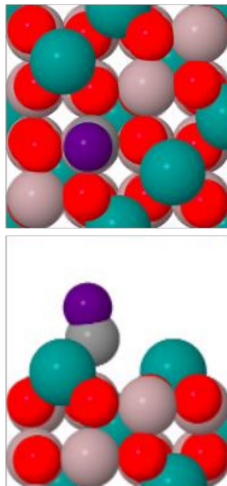
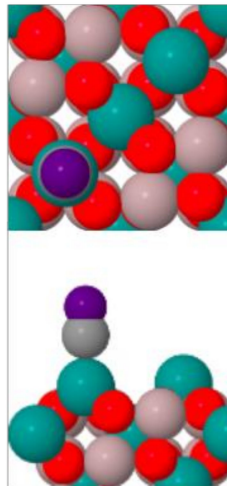
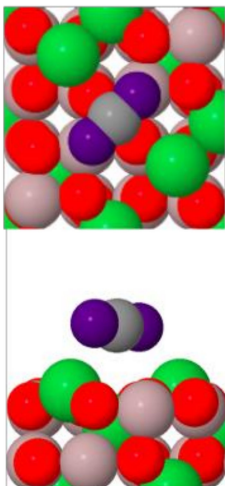
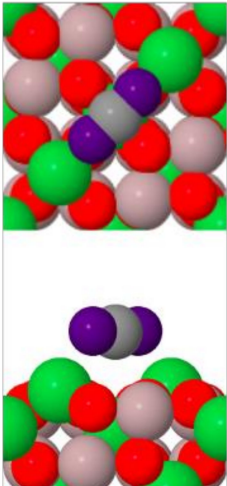
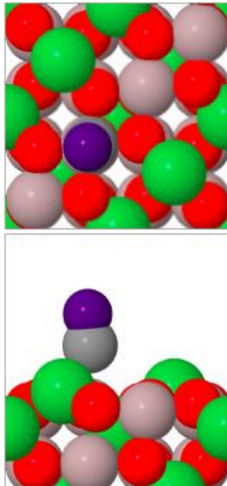
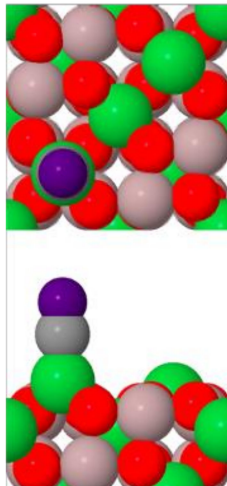
(a)	(b)	(c)	(d)
			
$E_{\text{ads}} = 75.3 \text{ kJ/mol}$	$E_{\text{ads}} = 162.9 \text{ kJ/mol}$	$E_{\text{ads}} = 30.8 \text{ kJ/mol}$	$E_{\text{ads}} = 59.7 \text{ kJ/mol}$
(e)	(f)	(g)	(h)
			
$E_{\text{ads}} = 15.5 \text{ kJ/mol}$	$E_{\text{ads}} = 36.5 \text{ kJ/mol}$	$E_{\text{ads}} = 16.9 \text{ kJ/mol}$	$E_{\text{ads}} = 179.8 \text{ kJ/mol}$

Figure 5. Top and side views of adsorbed CO₂ and CO on MgAl₂O₄(100) (a–d) and NiAl₂O₄(100) (e–h). DFT-predicted adsorption energies are provided below each figure. Dark grey and purple atoms are carbon of CO and oxygen of CO, respectively. The colors for other atoms are described in Figure 1.

In terms of NiAl₂O₄(100), our simulation predicts that CO₂ binds weakly to its surface with adsorption energies of 15.5 kJ/mol and 36.5 kJ/mol on Al_{cus} and Mg_{cus} sites, respectively (Figure 5). In addition, we tested bent CO₂ configurations on both sites, and found that bent CO₂ transformed to linear CO₂ during DFT relaxations, which is the opposite of that observed for MgAl₂O₄(100). These results imply that CO₂ experiences strong repulsive interactions during adsorption on NiAl₂O₄(100), which cause weak binding of the adsorbed CO₂. In contrast, adsorbed CO binds strongly to NiAl₂O₄(100). CO strongly and stably interacted with Ni_{cus} sites with an adsorption energy of 179.8 kJ/mol, but only interacted weakly on Al_{cus} sites. Accordingly, the order of the predicted stabilities of CO₂ and CO on NiAl₂O₄(100) contrasted with that on MgAl₂O₄. Overall, our computational

results confirm that the experimentally observed higher selectivity toward CO for CO₂ methanation on MgAl₂O₄ stems from the low stability of adsorbed CO, which leads to facile CO desorption during the methanation reaction

During catalytic reactions, surfaces are not pristine because of on-going oxidation and reduction reactions. Thus, catalytic surfaces have edges, kinks, and some reduced sites, and these features have been proposed to be highly active because they are coordinatively more saturated [39–42]. To consider these effects during CO₂ methanation, we assume that the effects of oxygen vacancies (Ov) can be representative of the effects of reduced sites, which would provide initial insights for the effects of reduced sites. We first checked the Ov formation energy to evaluate the thermodynamic feasibility of Ov formation on the (100) surfaces [39]. The predicted Ov formation energies were 589 kJ/mol for MgAl₂O₄(100) and 414 kJ/mol for NiAl₂O₄(100). This implies that Ov rarely forms on both surfaces thermodynamically. Despite the less favorable Ov formation, the oxygen vacancies still can be kinetically generated by surface reactions with carbon species from the CO₂ methanation process. Therefore, we tested the effects of adjacent oxygen vacancies on the stabilities of CO₂ and CO on MgAl₂O₄(100) and NiAl₂O₄(100) surfaces by removing a surface oxygen adjacent to adsorbates.

Our simulations predicted that the presence of an oxygen vacancy would significantly stabilize adsorbed CO and CO₂ on MgAl₂O₄(100) and NiAl₂O₄(100) for most cases (Table 2). On MgAl₂O₄(100), CO stability on the Al_{cus} site is enhanced with an adjacent oxygen vacancy by ~ 57 kJ/mol, but this is still too low to effectively prevent CO desorption during methanation. In contrast to MgAl₂O₄, we found that CO on Al_{cus} sites in the presence of Ov is not stable on NiAl₂O₄; CO on Al_{cus} sites with Ov was found to migrate to Ni_{cus} sites during DFT relaxation. On Ni_{cus} sites, the presence of Ov improves CO stability by ~ 40 kJ/mol. Based on these results, we conclude that the presence of oxygen vacancies influences the surface stabilities of CO and CO₂ on MgAl₂O₄(100) and NiAl₂O₄(100), but that the effect of Ov on the stability of CO on MgAl₂O₄(100) is not enough to secure adsorbed CO during methanation, which suggests that CO selectivity would not be considerably changed by the presence of surface defects.

Table 2. Adsorption energies of CO₂ and CO on MgAl₂O₄(100) and NiAl₂O₄(100) with and without adjacent oxygen vacancies.

Adsorbed Molecule	MgAl ₂ O ₄				NiAl ₂ O ₄			
	Al _{cus}		Mg _{cus}		Al _{cus}		Ni _{cus}	
	0 Ov	1 Ov	0 Ov	1 Ov	0 Ov	1 Ov	0 Ov	1 Ov
CO	30.8	87.9	59.7	57.8	16.9	-	179.8	233.1
CO ₂	75.3	187.1	162.9	138.3	7.9	68.3	36.5	−4.6

4.2. Electronic Analysis of the Stability of Adsorbed CO

To determine the reasons for the different stabilities of CO on MgAl₂O₄, we conducted pCOHP analysis between CO molecules and the cus sites of Mg and Ni [27–29]. Integrated pCOHP (IpCOHP), obtained by integrating the pCOHP up to the Fermi level, allowed us to separately evaluate bonding and antibonding contributions to CO stability. Table 3 shows the IpCOHP results for CO–Mg_{cus}, and CO–Ni_{cus}. Results show that CO and Ni_{cus} have much higher total bonding interactions than CO and Mg_{cus}. For *s* and *p* orbitals, weak bonding and strong antibonding interactions, and thus, weak total bonding interactions, were predicted for CO–Mg_{cus}. The CO–Ni_{cus} interaction was predicted to involve strong bonding and weak antibonding interactions. In addition, the presence of *d* orbitals of the Ni_{cus} site was found to strongly contribute to the bonding interaction (−3.58), whereas no *d* orbitals were present at the Mg_{cus} site. We believe that the weaker bonding and stronger antibonding for *s* and *p* orbitals and the absence of *d* orbital is why adsorbed CO on MgAl₂O₄ tends to desorb from Mg_{cus} site.

Table 3. IpCOHP results for CO-Mg_{cus}, and CO-Ni_{cus}.

Bonding Types	MgAl ₂ O ₄			NiAl ₂ O ₄		
	Mg _{cus}			Ni _{cus}		
	<i>s, p</i>	<i>d</i>	<i>s, p, d</i>	<i>s, p</i>	<i>d</i>	<i>s, p, d</i>
Bonding	−2.08	−	−2.08	−2.68	−3.58	−6.26
Anti-Bonding	0.36	−	0.36	0.31	1.11	1.42
Total Bonding	−1.72	−	−1.72	−2.37	−2.47	−4.83

4.3. C–O Bond-Breaking Kinetics

In this section, we focus on C–O bond cleavage of CO₂ and CO to generate the carbon that subsequently undergoes hydrogenation to form CH₄. Energy diagrams of C–O bond cleavages on MgAl₂O₄(100) and NiAl₂O₄(100) are shown in Figure 6a. The proposed mechanism is based on the most favorable configurations of CO₂ on both surfaces, meaning that CO₂ is on the Mg_{cus} site of MgAl₂O₄ and on the Ni_{cus} site of NiAl₂O₄. C–O bond cleavages of CO₂ on the Al_{cus} site were also examined (not shown) but were predicted to be energetically less favorable than cleavages on Mg_{cus} and Ni_{cus} sites. Our results show that the overall C–O bond cleavage from CO₂ to C is endothermic on pristine MgAl₂O₄(100) and NiAl₂O₄(100), and that cleavage requires 715 kJ/mol and 578 kJ/mol for MgAl₂O₄ and NiAl₂O₄, respectively. These results indicate that the overall C–O bond cleavage on both substrates requires high temperatures to overcome unfavorable thermodynamics. We also found that C–O bond cleavage of CO₂ (CO) on MgAl₂O₄ had negligible reverse barriers, i.e., CO* and O* (C* and O*) are predicted to readily recombine. The C–O bond cleavage of CO₂ on NiAl₂O₄(100) had a relatively small barrier of 127.2 kJ/mol and a reverse barrier of 26.6 kJ/mol, and C–O bond cleavage of CO also had a negligible reverse barrier, which is similar to that of MgAl₂O₄. It should be noted that the CO desorption energy is much smaller than the energy required to cleave the C–O bond of CO (30–60 kJ/mol vs. 622 kJ/mol) on MgAl₂O₄(100), which implies that the CO desorption rate would be much faster than the C–O cleavage rate regardless of prefactors. Again, these results agree well with the experimentally observed high CO selectivity of MgAl₂O₄. Overall, DFT-predicted large energy barriers for C–O cleavages and negligible reverse barriers on Mg_{cus} and Ni_{cus} sites suggest that methanation kinetics via C–O bond cleavage on pristine surfaces are energetically and kinetically unfavorable, and thus, would require high temperatures.

We also evaluated the kinetics of C–O bond cleavage on reduced surfaces of MgAl₂O₄(100) and NiAl₂O₄(100) with an oxygen vacancy. Figure 6b provides energy diagrams of C–O bond cleavage on both surfaces. Again, results were obtained using the most stable configurations for CO₂ and CO on Mg_{cus} (MgAl₂O₄) and Ni_{cus} (NiAl₂O₄) sites. The kinetics of C–O bond cleavage in CO₂ on the Al_{cus} site was also investigated (details not shown), but the kinetics were found to be energetically less favorable than those at Mg_{cus} and Ni_{cus} sites. From the simulations, we found that the oxygen vacancy was healed by an oxygen generated from C–O bond breaking from CO₂ to CO on both surfaces and that bond breaking on MgAl₂O₄ requires much lower energy compared to the NiAl₂O₄. The CO₂ bond cleavage on reduced MgAl₂O₄(100) was predicted to be exothermic (207.4 kJ/mol), but that on reduced NiAl₂O₄(100) was predicted to be endothermic (693.6 kJ/mol). Kinetic enhancement by adjacent oxygen vacancies has been reported for transition metal oxides [39,40,43]. In particular, on PdO(101), oxygen vacancies were found to impact CO oxidation and thermal reduction kinetics significantly. Metal atoms adjacent to oxygen vacancies can abstract electrons, which modifies their electronic structures and influences surface reaction kinetics. We found the similar enhancements for MgAl₂O₄(100) but not for NiAl₂O₄(100) (Figure 6b). Although a single oxygen vacancy did not enhance the kinetics of overall C–O bond cleavage on NiAl₂O₄(100), the kinetics were significantly affected. Initial bond cleavage in the presence of adjacent Ov required the more energy than cleavage on a pristine surface, but subsequent bond cleavage in the presence of adjacent Ov required the less energy than the C–O bond cleavage of CO on a pristine surface. Based on these

results, we would expect that the presence of surface oxygen vacancies would strongly affect CO₂ methanation kinetics on MgAl₂O₄ and NiAl₂O₄ surfaces.

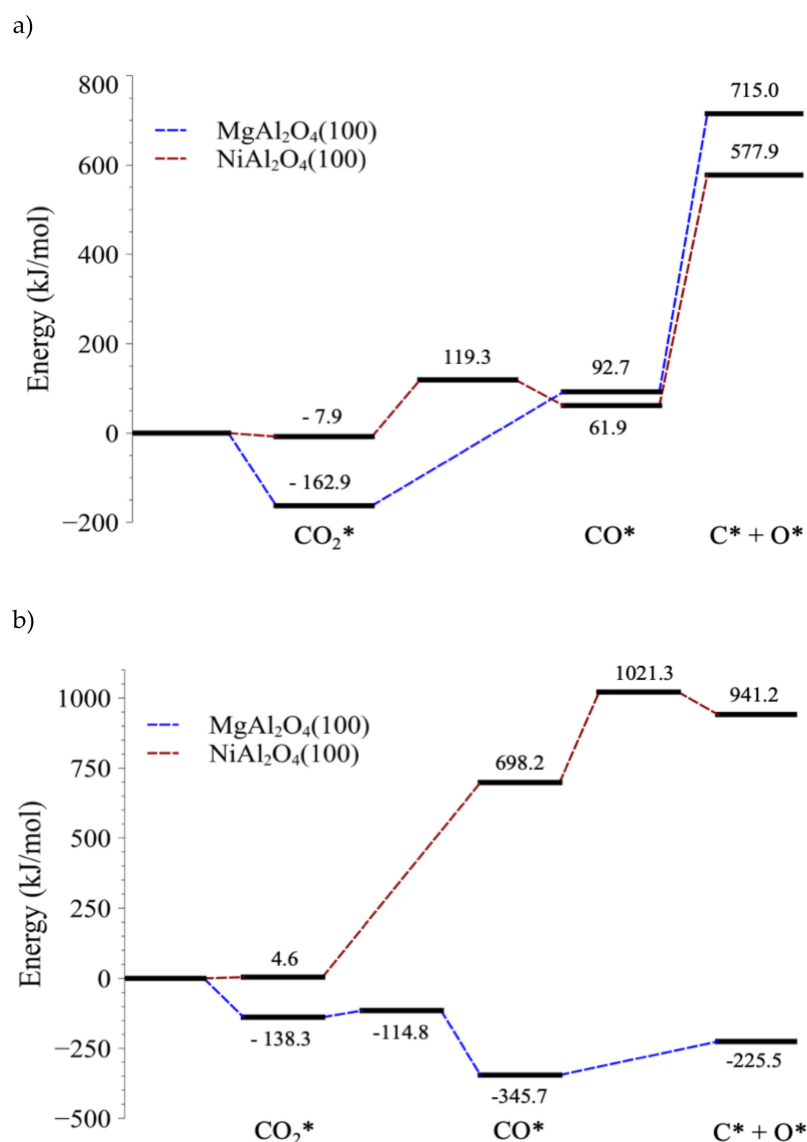


Figure 6. Energy diagrams of C–O bond cleavages for CO₂ and CO on (a) pristine and (b) defected surfaces. * represents adsorbed species on the surfaces (e.g., CO₂*: adsorbed CO₂ on the surface).

4.4. C–O Bond Cleavage of CO vs. C–O Bond Cleavage of CHO

In addition to the C–O bond cleavage of CO₂ and CO, many other potential C–O bond-breaking mechanisms may contribute to CH₄ generation, and one such mechanism is H-assisted CO₂ activations. On Ni-based catalysts, formate (CHOO) and carboxylate (COOH) pathways have been proposed, which provides kinetically and thermodynamically different preferences for the hydrogenation of CO₂ [44]. However, in this study, we focus on another potential pathway of C–O bond breaking from CHO on MgAl₂O₄(100) and NiAl₂O₄(100). After initial bond cleavage of CO₂, the generated CO reacts with adjacent H to form CHO, which undergoes C–O bond cleavage to produce CH. Such reactions would proceed if the kinetics and thermodynamics are more favorable than the other reactions paths. We evaluated the feasibilities of other potential mechanisms of C–O bond cleavage by focusing on the C–O bond cleavage of CHO. Simulations were performed on reduced surfaces because we had found earlier that the reduced surface enhances kinetics and adsorbate stabilities. Energy diagrams of C–O bond cleavage of CO vs. C–O bond cleavage

of CHO are provided in Figure 7. Results are based on the most stable configurations of CO and CHO on Mg_{cus} (MgAl_2O_4) and Ni_{cus} (NiAl_2O_4) sites. The simulation predicted that on $\text{NiAl}_2\text{O}_4(100)$, CHO formation from CO and H requires 165.7 kJ/mol, but that the C–O bond cleavage of CHO has a large energy barrier of ~232.9 kJ/mol (Figure 7a). The activation energy required to cleave the C–O bond of CHO is similar to that required to cleave CO, which suggests that on $\text{NiAl}_2\text{O}_4(100)$, C–O cleavage in CO and CHO would competitively occur due to the similar overall energies required. Energy diagrams of bond cleavages on reduced $\text{MgAl}_2\text{O}_4(100)$ are provided in Figure 7b, which show the different behaviors of C–O bond cleavage. Our results show that CHO formation is exothermic, with 339.9 kJ/mol, and that C–O bond cleavage in CHO has an activation energy of 192.4 kJ/mol and a negligible reverse energy requirement. The overall energy required to active the bond breaking is exothermic, but the C–O bond breaking from CHO is not. These results indicate that CO bond-breaking mechanisms from CHO would occur more readily than direct C–O bond breaking when surface defects are present. Based on the results obtained, we cannot conclusively establish that the C–O bond cleavage of CHO is the dominant pathway on reduced MgAl_2O_4 . Nevertheless, we believe that the alternative C–O cleavage pathways, including C–O bond cleavage in CHO, compete with direct C–O bond cleavage during methanation.

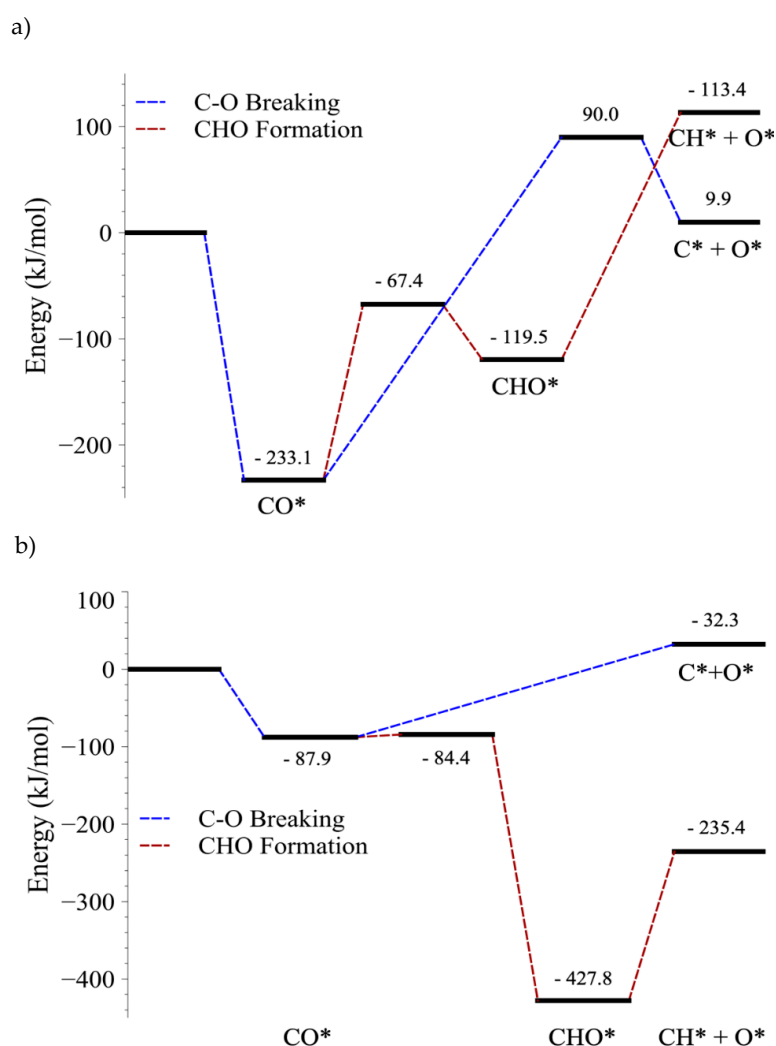


Figure 7. Energy diagrams of the direct C–O bond breaking ($\text{CO}^* \rightarrow \text{C} + \text{O}^*$) vs. indirect C–O bond breaking ($\text{CO}^* + \text{H}^* \rightarrow \text{CHO}^* \rightarrow \text{CH}^* + \text{O}^*$) on (a) defected $\text{NiAl}_2\text{O}_4(100)$ and (b) defected $\text{MgAl}_2\text{O}_4(100)$.

5. Conclusions

Mixtures of nickel–magnesium–alumina with different metal contents were investigated as CO₂ hydrogenation catalysts. A range of Ni_xMg_{1−x}Al₂O₄ spinels were produced (from $x = 0$ to 1) by co-precipitation. According to our experimental results for CO₂ hydrogenation over these catalysts, the reverse water gas shift reaction (CO₂ → CO) was preferred at high magnesium atomic ratios, and CO₂ methanation (CO₂ → CH₄) was favored by increasing nickel contents. To understand the kinetics for product selectivity of MgAl₂O₄ and NiAl₂O₄, we performed DFT calculations. Our simulation predicted that CO strongly adsorbs on the Ni_{cus} site of NiAl₂O₄; however, CO weakly adsorbs on the Mg_{cus} site of MgAl₂O₄ due to the weak total binding interactions within *s* and *p* orbitals, and the absence of a *d* orbital. The low stability of adsorbed CO on MgAl₂O₄ triggers CO desorption rather than undergoing further hydrogenation or C–O dissociation. As a result, the CO selectivity is higher on MgAl₂O₄ than NiAl₂O₄. Based on our experimental and computational results, the different reaction mechanisms on Ni_xMg_{1−x}Al₂O₄ spinels for CO₂ hydrogenation were revealed.

Author Contributions: Conceptualization, M.K., D.K. and N.-K.P.; Data curation, B.S. and E.H.K.; Investigation, B.S. and E.H.K.; Methodology, B.S., E.H.K. and J.B.; Supervision, M.K., D.K. and N.-K.P.; Validation B.S. and E.H.K.; Writing—original draft, B.S. and E.H.K.; Writing—review and editing, M.K., D.K. and N.-K.P. All authors have read and agreed to the published version of the manuscript.

Funding: This research was supported by the Basic Science Research Program through the National Re-search Foundation of Korea (NRF) funded by the Ministry of Education (2020R111A3051997), and the 2020 Yeungnam University Research Grant.

Conflicts of Interest: The authors declare no conflict of interest.

References

- Gielen, D.; Boshell, F.; Saygin, D.; Bazilian, M.D.; Wagner, N.; Gorini, R. The role of renewable energy in the global energy transformation. *Energy Strateg. Rev.* **2019**, *24*, 38–50. [\[CrossRef\]](#)
- Shen, W.; Chen, X.; Qiu, J.; Hayward, J.A.; Sayeef, S.; Osman, P.; Meng, K.; Dong, Z.Y. A comprehensive review of variable renewable energy levelized cost of electricity. *Renew. Sustain. Energy Rev.* **2020**, *133*, 110301. [\[CrossRef\]](#)
- MacDowell, N.; Florin, N.; Buchard, A.; Hallett, J.; Galindo, A.; Jackson, G.; Adjiman, C.S.; Williams, C.K.; Shah, N.; Fennell, P. An overview of CO₂ capture technologies. *Energy Environ. Sci.* **2010**, *3*, 1645–1669. [\[CrossRef\]](#)
- Tapia, J.F.D.; Lee, J.-Y.; Ooi, R.E.H.; Foo, D.C.Y.; Tan, R.R. A review of optimization and decision-making models for the planning of CO₂ capture, utilization and storage (CCUS) systems. *Sustain. Prod. Consum.* **2018**, *13*, 1–15. [\[CrossRef\]](#)
- Rönsch, S.; Schneider, J.; Matthischke, S.; Schlüter, M.; Götz, M.; Lefebvre, J.; Prabhakaran, P.; Bajohr, S. Review on methanation—From fundamentals to current projects. *Fuel* **2016**, *166*, 276–296. [\[CrossRef\]](#)
- Daza, Y.A.; Kuhn, J.N. CO₂ conversion by reverse water gas shift catalysis: Comparison of catalysts, mechanisms and their consequences for CO₂ conversion to liquid fuels. *RSC Adv.* **2016**, *6*, 49675–49691. [\[CrossRef\]](#)
- Hernandez Lalinde, J.A.; Roongruangsree, P.; Ilseemann, J.; Bäumer, M.; Kopyscinski, J. CO₂ methanation and reverse water gas shift reaction. Kinetic study based on in situ spatially-resolved measurements. *Chem. Eng. J.* **2020**, *390*, 124629. [\[CrossRef\]](#)
- Mills, G.A.; Steffgen, F.W. Catalytic Methanation. *Catal. Rev.* **1974**, *8*, 159–210. [\[CrossRef\]](#)
- Kirchner, J.; Baysal, Z.; Kureti, S. Activity and Structural Changes of Fe-based Catalysts during CO₂ Hydrogenation towards CH₄—A Mini Review. *ChemCatChem* **2020**, *12*, 981–988. [\[CrossRef\]](#)
- Wu, H.C.; Chang, Y.C.; Wu, J.H.; Lin, J.H.; Lin, I.K.; Chen, C.S. Methanation of CO₂ and reverse water gas shift reactions on Ni/SiO₂ catalysts: The influence of particle size on selectivity and reaction pathway. *Catal. Sci. Technol.* **2015**, *5*, 4154–4163. [\[CrossRef\]](#)
- Chen, C.-S.; Budi, C.S.; Wu, H.-C.; Saikia, D.; Kao, H.-M. Size-Tunable Ni Nanoparticles Supported on Surface-Modified, Cage-Type Mesoporous Silica as Highly Active Catalysts for CO₂ Hydrogenation. *ACS Catal.* **2017**, *7*, 8367–8381. [\[CrossRef\]](#)
- Aziz, M.A.A.; Jalil, A.A.; Triwahyono, S.; Mukti, R.R.; Taufiq-Yap, Y.H.; Sazegar, M.R. Highly active Ni-promoted mesostructured silica nanoparticles for CO₂ methanation. *Appl. Catal. B Environ.* **2014**, *147*, 359–368. [\[CrossRef\]](#)
- Solymosi, F.; Erdöhelyi, A.; Bánsági, T. Methanation of CO₂ on supported rhodium catalyst. *J. Catal.* **1981**, *68*, 371–382. [\[CrossRef\]](#)
- Weatherbee, G.D.; Bartholomew, C.H. Hydrogenation of CO₂ on group VIII metals: II. Kinetics and mechanism of CO₂ hydrogenation on nickel. *J. Catal.* **1982**, *77*, 460–472. [\[CrossRef\]](#)

15. Yang Lim, J.; McGregor, J.; Sederman, A.J.; Dennis, J.S. Kinetic studies of CO₂ methanation over a Ni/ γ -Al₂O₃ catalyst using a batch reactor. *Chem. Eng. Sci.* **2016**, *141*, 28–45. [\[CrossRef\]](#)
16. Kwon, B.C.; Park, N.-K.; Kang, M.; Kang, D.; Seo, M.W.; Lee, D.; Jeon, S.G.; Ryu, H.-J. CO₂ hydrogenation activity of Ni-Mg-Al₂O₃ catalysts: Reaction behavior on NiAl₂O₄ and MgAl₂O₄. *Korean J. Chem. Eng.* **2021**, *38*, 1188–1196. [\[CrossRef\]](#)
17. Stangeland, K.; Kalai, D.; Li, H.; Yu, Z. CO₂ Methanation: The Effect of Catalysts and Reaction Conditions. *Energy Procedia* **2017**, *105*, 2022–2027. [\[CrossRef\]](#)
18. Karam, L.; Bacariza, M.C.; Lopes, J.M.; Henriques, C.; Massiani, P.; El Hassan, N. Assessing the potential of xNi-yMg-Al₂O₃ catalysts prepared by EISA-one-pot synthesis towards CO₂ methanation: An overall study. *Int. J. Hydrogen Energy* **2020**, *45*, 28626–28639. [\[CrossRef\]](#)
19. Galhardo, T.S.; Braga, A.H.; Arpini, B.H.; Szanyi, J.; Gonçalves, R.V.; Zornio, B.F.; Miranda, C.R.; Rossi, L.M. Optimizing Active Sites for High CO Selectivity during CO₂ Hydrogenation over Supported Nickel Catalysts. *J. Am. Chem. Soc.* **2021**, *143*, 4268–4280. [\[CrossRef\]](#) [\[PubMed\]](#)
20. Zhang, S.; Ying, M.; Yu, J.; Zhan, W.; Wang, L.; Guo, Y.; Guo, Y. Ni_xAl₁₁O₂- δ mesoporous catalysts for dry reforming of methane: The special role of NiAl₂O₄ spinel phase and its reaction mechanism. *Appl. Catal. B Environ.* **2021**, *291*, 120074. [\[CrossRef\]](#)
21. Blöchl, P.E. Projector augmented-wave method. *Phys. Rev. B* **1994**, *50*, 17953–17979. [\[CrossRef\]](#)
22. Kresse, G.; Hafner, J. *Ab initio* molecular dynamics for liquid metals. *Phys. Rev. B* **1993**, *47*, 558. [\[CrossRef\]](#) [\[PubMed\]](#)
23. Perdew, J.P.; Ernzerhof, M.; Burke, K. Rationale for mixing exact exchange with density functional approximations. *J. Chem. Phys.* **1996**, *105*, 9982–9985. [\[CrossRef\]](#)
24. Grimme, S.; Antony, J.; Ehrlich, S.; Krieg, H. A consistent and accurate *ab initio* parametrization of density functional dispersion correction (DFT-D) for the 94 elements H-Pu. *J. Chem. Phys.* **2010**, *132*, 154104. [\[CrossRef\]](#) [\[PubMed\]](#)
25. Hasan, M.M.; Dholabhai, P.P.; Castro, R.H.R.; Uberuaga, B.P. Stabilization of MgAl₂O₄ spinel surfaces via doping. *Surf. Sci.* **2016**, *649*, 138–145. [\[CrossRef\]](#)
26. Henkelman, G.; Uberuaga, B.P.; Jónsson, H. A climbing image nudged elastic band method for finding saddle points and minimum energy paths. *J. Chem. Phys.* **2000**, *113*, 9901–9904. [\[CrossRef\]](#)
27. Deringer, V.L.; Tchougréeff, A.L.; Dronskowski, R. Crystal orbital Hamilton population (COHP) analysis as projected from plane-wave basis sets. *J. Phys. Chem. A* **2011**, *115*, 5461–5466. [\[CrossRef\]](#)
28. Dronskowski, R.; Blöchl, P.E. Crystal orbital hamilton populations (COHP). Energy-resolved visualization of chemical bonding in solids based on density-functional calculations. *J. Phys. Chem.* **1993**, *97*, 8617–8624. [\[CrossRef\]](#)
29. Maintz, S.; Deringer, V.L.; Tchougréeff, A.L.; Dronskowski, R. Analytic projection from plane-wave and PAW wavefunctions and application to chemical-bonding analysis in solids. *J. Comput. Chem.* **2013**, *34*, 2557–2567. [\[CrossRef\]](#)
30. Maintz, S.; Deringer, V.L.; Tchougréeff, A.L.; Dronskowski, R. LOBSTER: A tool to extract chemical bonding from plane-wave based DFT. *J. Comput. Chem.* **2016**, *37*, 1030–1035. [\[CrossRef\]](#)
31. Ashok, J.; Raju, G.; Reddy, P.S.; Subrahmanyam, M.; Venugopal, A. Catalytic decomposition of CH₄ over NiO-Al₂O₃-SiO₂ catalysts: Influence of catalyst preparation conditions on the production of H₂. *Int. J. Hydrogen Energy* **2008**, *33*, 4809–4818. [\[CrossRef\]](#)
32. Vesselli, E.; Schweicher, J.; Bundhoo, A.; Frennet, A.; Kruse, N. Catalytic CO₂ Hydrogenation on Nickel: Novel Insight by Chemical Transient Kinetics. *J. Phys. Chem. C* **2011**, *115*, 1255–1260. [\[CrossRef\]](#)
33. Hinojosa, J.A.; Antony, A.; Hakanoglu, C.; Asthagiri, A.; Weaver, J.F. Adsorption of CO₂ on a PdO(101) Thin Film. *J. Phys. Chem. C* **2012**, *116*, 3007–3016. [\[CrossRef\]](#)
34. Thompson, T.L.; Diwald, O.; Yates, J.T. CO₂ as a Probe for Monitoring the Surface Defects on TiO₂(110) Temperature-Programmed Desorption. *J. Phys. Chem. B* **2003**, *107*, 11700–11704. [\[CrossRef\]](#)
35. Henderson, M.A.; Epling, W.S.; Perkins, C.L.; Peden, C.H.F.; Diebold, U. Interaction of Molecular Oxygen with the Vacuum-Annealed TiO₂(110) Surface: Molecular and Dissociative Channels. *J. Phys. Chem. B* **1999**, *103*, 5328–5337. [\[CrossRef\]](#)
36. Wang, Y.; Lafosse, A.; Jacobi, K. Adsorption and Reaction of CO₂ on the RuO₂(110) Surface. *J. Phys. Chem. B* **2002**, *106*, 5476–5482. [\[CrossRef\]](#)
37. Lafosse, A.; Wang, Y.; Jacobi, K. Carbonate formation on the O-enriched RuO₂(110) surface. *J. Chem. Phys.* **2002**, *117*, 2823–2831. [\[CrossRef\]](#)
38. Seiferth, O.; Wolter, K.; Dillmann, B.; Klivenyi, G.; Freund, H.J.; Scarano, D.; Zecchina, A. IR investigations of CO₂ adsorption on chromia surfaces: Cr₂O₃ (0001)/Cr(110) versus polycrystalline α -Cr₂O₃. *Surf. Sci.* **1999**, *421*, 176–190. [\[CrossRef\]](#)
39. Kim, M.; Pan, L.; Weaver, J.F.; Asthagiri, A. Initial Reduction of the PdO(101) Surface: Role of Oxygen Vacancy Formation Kinetics. *J. Phys. Chem. C* **2018**, *122*, 26007–26017. [\[CrossRef\]](#)
40. Zhang, F.; Pan, L.; Li, T.; Diulus, J.T.; Asthagiri, A.; Weaver, J.F. CO Oxidation on PdO(101) during Temperature-Programmed Reaction Spectroscopy: Role of Oxygen Vacancies. *J. Phys. Chem. C* **2014**, *118*, 28647–28661. [\[CrossRef\]](#)
41. Van Den Bossche, M.; Grönbeck, H. Methane Oxidation over PdO(101) Revealed by First-Principles Kinetic Modeling. *J. Am. Chem. Soc.* **2015**, *137*, 12035–12044. [\[CrossRef\]](#)
42. Chin, Y.C.; Garcia-Dieguez, M.; Iglesia, E. Dynamics and Thermodynamics of Pd–PdO Phase Transitions: Effects of Pd Cluster Size and Kinetic Implications for Catalytic Methane Combustion. *J. Phys. Chem. C* **2016**, *120*, 1446–1460. [\[CrossRef\]](#)

-
43. Schilling, A.C.; Groden, K.; Simonovis, J.P.; Hunt, A.; Hannagan, R.T.; Çınar, V.; McEwen, J.S.; Sykes, E.C.H.; Waluyo, I. Accelerated Cu₂O Reduction by Single Pt Atoms at the Metal-Oxide Interface. *ACS Catal.* **2020**, *10*, 4215–4226. [[CrossRef](#)]
 44. Vogt, C.; Monai, M.; Sterk, E.B.; Palle, J.; Melcherts, A.E.M.; Zijlstra, B.; Groeneveld, E.; Berben, P.H.; Boereboom, J.M.; Hensen, E.J.M.; et al. Understanding carbon dioxide activation and carbon–carbon coupling over nickel. *Nat. Commun.* **2019**, *10*, 5330. [[CrossRef](#)] [[PubMed](#)]